Measured and calculated K-fluorescence effects on the MTF of an amorphous-selenium based CCD x-ray detector

David M. Hunter[a]
Sunnybrook Health Sciences Centre, SG-17, 2075 Bayview Avenue, Toronto, Ontario, M4N 3M5, Canada

George Belev
Canadian Light Source, Inc., University of Saskatchewan, 101 Perimeter Road, Saskatoon, Saskatchewan K, S7N 0X4, Canada

Safa Kasap
Department of Electrical and Computer Engineering, University of Saskatchewan, 57 Campus Drive, Saskatoon, Saskatchewan, S7N 5A9, Canada

Martin J. Yaffe
Sunnybrook Health Sciences Centre, S6-57, 2075 Bayview Avenue, Toronto, Ontario, M4N 3M5 and Department of Medical Biophysics, University of Toronto, Ontario, M4N 3M5, Canada

Purpose: Theoretical reasoning suggests that direct conversion digital x-ray detectors based upon photoconductive amorphous-selenium (a-Se) could attain very high values of the MTF (modulation transfer function) at spatial frequencies well beyond 20 cycles mm^{-1}. One of the fundamental factors affecting resolution loss, particularly at x-ray energies just above the K-edge of selenium (12.66 keV), is the K-fluorescence reabsorption mechanism, wherein energy can be deposited in the detector at locations laterally displaced from the initial x-ray interaction site. This paper compares measured MTF changes above and below the Se K-edge of a CCD based a-Se x-ray detector with theoretical expectations.

Methods: A prototype 25 μm sampling pitch (Nyquist frequency = 20 cycles mm^{-1}, 200 μm thick a-Se layer based x-ray detector, utilizing a specialized CCD readout device (200 × 400 area array), was used to make edge images with monochromatic x-rays above and below the K-edge of Se. A vacuum double crystal monochromator, exposed to polychromatic x-rays from a synchrotron, formed the monochromatic x-ray source. The monochromaticity of the x-rays was 99% or better. The presampling MTF was determined using the slanted edge method. The theory modeling the MTF performance of the detector includes the basic x-ray interaction physics in the a-Se layer as well as effects related to the operation of the CCD and charge trapping at a blocking layer present at the CCD/a-Se interface.

Results: The MTF performance of the prototype a-Se CCD was reduced from the theoretical value prescribed by the basic Se x-ray interaction physics, principally by the presence of a blocking layer. Nevertheless, the K-fluorescence reduction in the MTF was observed, approximately as predicted by theory. For the CCD prototype detector, at five cycles mm^{-1}, there was a 14% reduction of the MTF, from a value of 0.7 below the K-edge of Se, to 0.6 just above the K-edge.

Conclusions: The MTF of an a-Se x-ray detector has been measured using monochromatic x-rays above and below the K-edge of selenium. The MTF is poorer above the K-edge by an amount consistent with theoretical expectations. © 2012 American Association of Physicists in Medicine. [DOI: 10.1118/1.3673957]

Key words: x-ray, MTF, resolution, K-fluorescence, selenium, photoconductor, CCD

I. INTRODUCTION

The use of a-Se as a direct detection material for digital mammography is now well established, with the smallest sampling pitch currently in widespread use being 70 μm, for a Nyquist frequency, ν_N, = 7.1 cycles mm^{-1}. A 50 μm (ν_N = 10 cycles mm^{-1}) sampling pitch a-Se system[1] based upon photo-optical readout has recently been introduced. Also, a new a-Se detector with a 150 μm sampling pitch for lower resolution applications such as chest imaging[2] is commercially available. However, the full potential of a-Se as a

detector material for high resolution x-ray imaging has not yet been realized. Theoretical studies have shown that a-Se could provide an appreciable spatial frequency response up to 50 cycles mm^{-1} or higher.[3] Higher resolution x-ray imaging devices could have application in mammography, biopsy sampling analysis, micro-CT, non destructive testing, and other possible x-ray imaging applications.

We previously reported[4] on the spatial frequency response of a single-line CCD a-Se prototype detector with a 25 μm sampling pitch. It was found that the frequency

response of the detector at higher spatial frequencies was quite sensitive to the thickness of the blocking layer that was used to limit the dark current in the device. In addition to the prototype single-line a-Se CCD readout device we have also developed a prototype small area a-Se CCD readout device, with a sampling pitch of 25 μm and a matrix size of 200×400. In this article, we present a complete theoretical analysis of the factors influencing the modulation transfer function (MTF). These factors are associated with x-ray interaction and energy transport in the detector material as well as phenomena related to the readout system. In particular, we validate experimentally the effects on MTF of K fluorescence reabsorption in a prototype detector over the energy range 11.5–30 keV.

II. THEORY

The spatial frequency response of a direct detection a-Se imaging device is affected by a number of different physical mechanisms related to the a-Se detection layer. These mechanisms include: (1) photoelectron range, (2) K-fluorescence reabsorption, (3) incoherent (Compton) scatter, (4) coherent (Rayleigh) scatter, (5) signal charge diffusion, (6) space charge effect, (7) electrostatic field blur effect caused by the charge trapping (blocking) layer at the signal detection plane, (8) a-Se signal lag, and (9) the obliquity of the incident x-rays to the a-Se layer. The general theory concerning factors affecting the resolution of a-Se was first addressed in depth by Que and Rowlands[3] and our analysis closely follows on that work. Factors 5 and 6 are practically insignificant according to Refs. 3 and 5). More recently, numerous papers[6–9] by other authors have been written addressing the signal and noise transfer properties in x-ray photoconductors such as a-Se, and Pb compounds including PbI, and PbO. With respect to a-Se detectors, the analyses have mainly focused on the effects on the reduction of MTF associated with K-fluorescence at low energies ($E < 20$ keV) while not considering in detail effects at energies above 80 keV where the MTF becomes increasingly compromised by the range of photoelectrons. These studies were largely limited to theoretical analysis.

In practice there can be a number of other factors reducing the frequency response which are related to the readout device itself and not the a-Se layer. For the small prototype CCD readout device we used, the additional factors are the CCD charge transfer efficiency, CTE, and charge transfer lag λ_{MOS} in the MOSFET switches.

The intrinsic x-ray signal generation processes (energy transfer) in a x-ray photoconductor are linear and additive so the final weighted MTF_w associated with the a-Se layer can be expressed as

$$
\begin{aligned}
MTF_w = {} & w_{pe}MTF_{pe} + w_\alpha MTF_\alpha + w_\beta MTF_\beta \\
& + w_{Auger}MTF_{Auger} + w_c MTF_c \\
& + w_{coh}MTF_{coh},
\end{aligned}
\tag{1}
$$

where the weighting factors for fractional energy distribution and the MTF components on the right hand side of the equation are, respectively, associated with the photoelectric

electron kinetic energy $T = h\nu_X - E_K$ (h is Planck's constant, ν_X is the x-ray frequency, and E_K is the K-shell binding energy), photoelectric stimulated K_α and K_β fluorescent emission, Compton scattering, and coherent scattering. Note that $w_{pe} + w_\alpha + w_\beta + w_{Auger} + w_c + w_{coh} = 1.0$. Each of the separate MTFs is scaled to 1 near zero spatial frequency. In the case of elastic coherent scattering the energy transfer process is assumed to occur when the scattered photon is subsequently absorbed by a photoelectric interaction and it is assumed all of the absorbed energy is deposited at the photoelectric interaction site. This assumption is true to a high degree of approximation at the low x-ray energies (<20 keV) where the coherent cross section is largest and the photoelectron range is very short. Compton scattered photons are also assumed to be absorbed by a subsequent photelectric process. The effect of Compton scattered electrons has not been directly accounted for in our model. The maximum kinetic energy imparted to an electron in a Compton scattering process is $h\nu_X\left(\frac{2\alpha_0}{1+2\alpha_0}\right)$ where $\alpha = \frac{h\nu_X}{m_0 c^2}$, c is the speed of light, and m_0 is the rest mass of the electron. For a 100 keV photon, the maximum Compton scattered electron energy is about 28 keV. Using the methods given in Appendix A this corresponds to an effective range of about $\sim\left[\frac{6.5}{4} = 1.6\right]$ μm. For both coherent and Compton scattering, only single scattering events are considered.

As an example of an energy weighting fraction, w_α the energy fraction deposited by K_α fluorescence, is given by

$$
w_\alpha = P_\alpha P_k Y_f R_{pe} \frac{E_\alpha}{E} f_\alpha,
\tag{2}
$$

where P_α is the probability of a K_α emission (given that a K shell electron has been ejected by a photoelectric interaction), P_k is the K shell participation fraction, Y_f is K-fluorescence yield (competing with Auger-electron emission), R_{pe} is the ratio of the attenuation coefficient due to photoelectric interactions to the total attenuation coefficient, $\frac{E_\alpha}{E}$ is the ratio of the fluorescent energy to the incident photon energy E, and f_α is the fraction of the K_α emission which is reabsorbed in the a-Se layer. A similar equation exists for K_β fluorescence. In this paper, we ignore the other pathways involving the L, M shells, and thus, we take $P_\alpha + P_\beta = 1$. The Auger-electron weighting factor is given by

$$
w_{Auger} = P_k(1 - Y_f)R_{pe} \frac{E_K}{E}.
\tag{3}
$$

The K shell participation fraction P_K can be given by

$$
P_K(h\nu_X) = \frac{\tau_{aboveK}(h\nu_X) - \tau_{belowK}(h\nu_X)}{\tau_{aboveK}(h\nu_X)}
\tag{4}
$$

where τ_{aboveK} and τ_{belowK} are the photoelectric attenuation coefficients above and below the K – edge of the detector x-ray absorber. In the literature, normally only two energies are used to calculate P_K and it is assumed not to be a function of energy. In our calculations we also have used a single value of P_K evaluated at the K-edge. However it cannot be assumed that the value of the K-shell participation factor
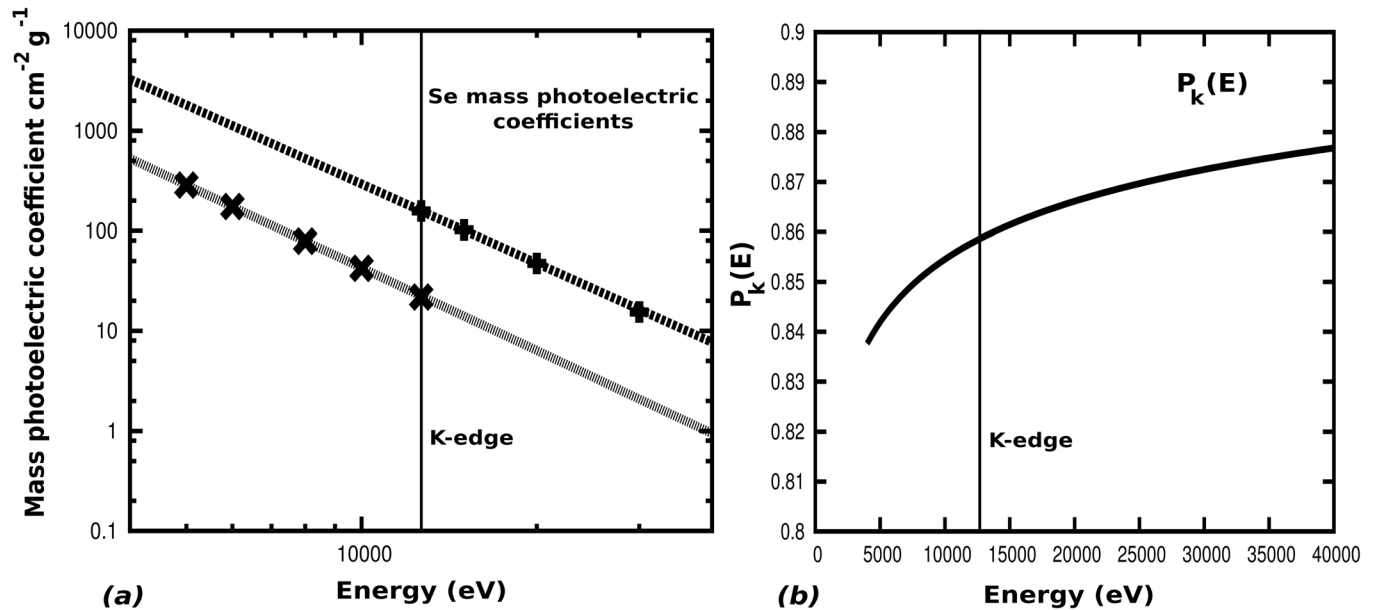
FIG. 1. Theoretical fits of mass photoelectric coefficients above and below the *K*-edge are shown in (a). An estimation of the *K*-shell participation factor $P_K(h\nu_X)$ is shown in (b).

will remain constant for energies above the *K*-edge. From a theoretical analysis[10] for the *K*-shell, the photoelectric absorption coefficient τ_K is expected to be of the form

$$\tau_K = N\phi_0 \frac{Z^5}{137^4} 4\sqrt{2}\left(\frac{m_0 c^2}{h\nu_X}\right)^{\frac{7}{2}}, \tag{5}$$

where N is the number of atoms per cm^3, and ϕ_0 is the classical Thomson scattering cross section. It can be expected that a similar form exists for the *L*, *M* shells. Empirical data on photoelectric coefficients below the K binding energy were fit to an equation of this form (i.e., a power law dependence on energy) and similarly data above the K binding energy were separately fit to such an equation. These curves were extrapolated to estimate τ_{L+M} and $\tau_{L+M} + \tau_K$ as in Fig. 1(a). These were then used to estimate the *K*-shell participation factor as a function of energy as shown in Fig. 1(b). The values of the exponents were -2.75 below the *K*-edge and -2.62 above the *K*-edge compared to the simple theoretical expectation from Eq. (5) of -3.5. The estimated variation of $P_K(h\nu_X)$ over the energy range of interest: 12.66–30 keV, is about 1.8%.

We will now proceed to consider specific terms in Eq. (1).

II.A. Photo-electron/auger-electron range

We evaluated, approximately, the MTF reducing effect of the range of photo-electrons and Auger-electrons. The energy of the photo-electrons (Auger-electrons) is $h\nu_X - E_K$ and (E_K, where E_K is the binding energy of the *K*-shell. Empirical fits of electron ranges and energy deposition curves, obtained from Monte Carlo simulations, have been carried out by Kim *et al.*[11] Our adaptation of their methods to determine the MTF reducing effects of free electrons created by

the absorption of x-rays is presented in Appendix A. We summarize the relevant findings here. Following Que and Rowlands, we assume the initial charge distribution formed by the release of the initial kinetic energy of the electron in three-space to be Gaussian given by $PSF(r)_{3D} = \exp\left(\frac{-r^2}{\sigma^2}\right)$, where r is the radial distance from the initial ionization location. The parameter σ is related to the energy deposition profile and is proportional to R_e, the extrapolated electron range (see Appendix A). The 3D electron charge is collected vertically by the electric field onto the 2D detector plane. Taking the 2D Fourier transform of $PSF(r)_{2D}$ we find that $MTF_{pe}(\nu) \propto \exp(-\pi^2\nu^2\sigma^2)$ where ν is the spatial frequency.

Applying the methods of Kim *et al.* we have found that for selenium that the ratio of R_{CSDA} (defined in Appendix A) to R_e is exactly 2.0. Furthermore, examining the energy deposition profiles (Appendix A), we have estimated that $\sigma \sim \frac{R_e}{2}$ which is equivalent to setting $\sigma \sim \frac{R_{CSDA}}{4}$. For the Auger-electrons we find that $R_{CSDA} = 1.72$ μm, and hence, $\sigma_{Auger} = 0.43$ μm. Therefore $MTF_{Auger}(\nu) \simeq 1.0$ for ν (0–20 cycles/mm). Shown plotted in Fig. 2 is $MTF_{pe}(\nu)$.

II.B. K-fluorescence reabsorption mechanism

Employing an analysis similar to that of Que and Rowlands and others,[3,7–9] the MTFs associated with the resolution reducing effects of the reabsorption of K-fluorescence radiation were computed by numerical methods. Specifically the MTFs associated with the K_α and K_β (11.21 and 12.50 keV, respectively) lines of selenium were calculated. In reality other fluorescent lines and transitions exist but they are of minor importance. These other possibilities (complex) have been elucidated and considered elsewhere.[8] The differences between the full model (complex) and the simple model (presented here) are reported by Hajdok *et al.*[8] to be
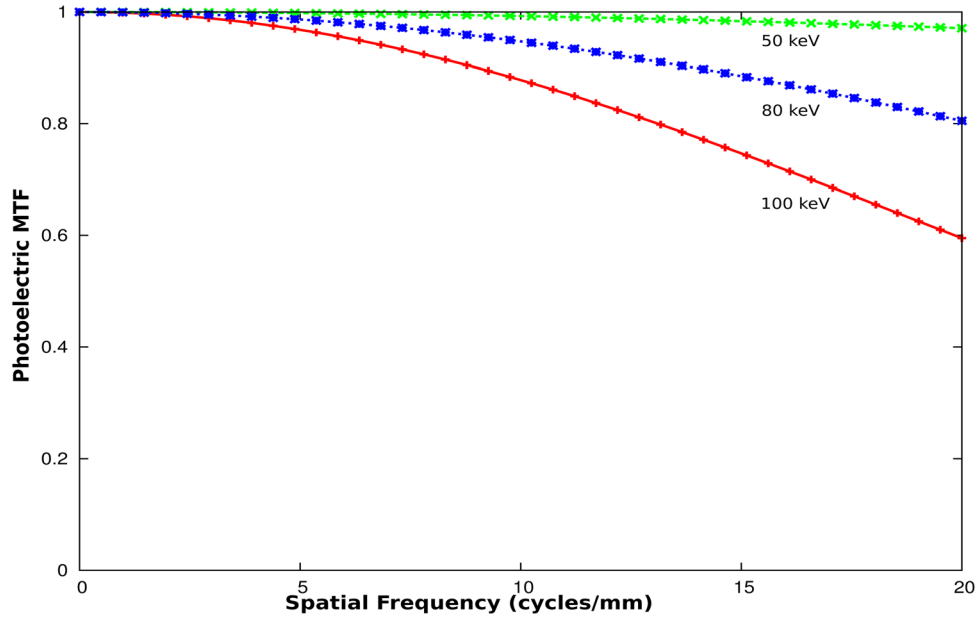
FIG. 2. The photoelectric MTF$_{pe}$ plotted for several different x-ray energies. It is not until energies exceed $\sim$80 keV that the range of the photoelectron significantly impacts resolution $\leq$20 cycles/mm. The plots do not include the effect of the sampling aperture.

at most 2%. This is approximately the same size of error introduced by assuming that P_K is constant. The geometry employed by our analysis is shown in Fig. 3. The fluorescent radiation is emitted isotropically and when it is reabsorbed, the charge created by its reabsorption is assumed to be collected vertically by the electric field $\mathcal{E}$ in the a-Se layer. Please refer to the paper by Que and Rowlands[3] for further details regarding the mathematics. The numerical limits of integration for the spatial calculations were from 0 to 10 mm. All of the MTF components were scaled to 1 at 0.1 cycles/mm, the lowest frequency obtainable, given that 10 mm was the maximum value of r in the numerical evaluations. Shown in Fig. 4 are the MTFs due to the reabsorption of K_α and K_β fluorescent radiation as we have calculated them.

II.C. Coherent and incoherent scatter

Shown in Fig. 5 is the coherent scattering differential cross section for several x-ray energies of interest. It is generally assumed that coherent scattering is of no consequence. However, we are primarily interested in observing a small change in the MTF near the K-edge of selenium, and this is where coherent scattering, will have its largest possible effect. Only single scattering events are considered. The physical model is similar to that for K-fluorescence as shown in Fig. 3 except that the scattering is not-isotropic but is distributed as shown in Fig. 5. After a coherent scattering event the photon is assumed to interact subsequently by the photoelectric effect at a second (absorption) location and all energy is assumed to be
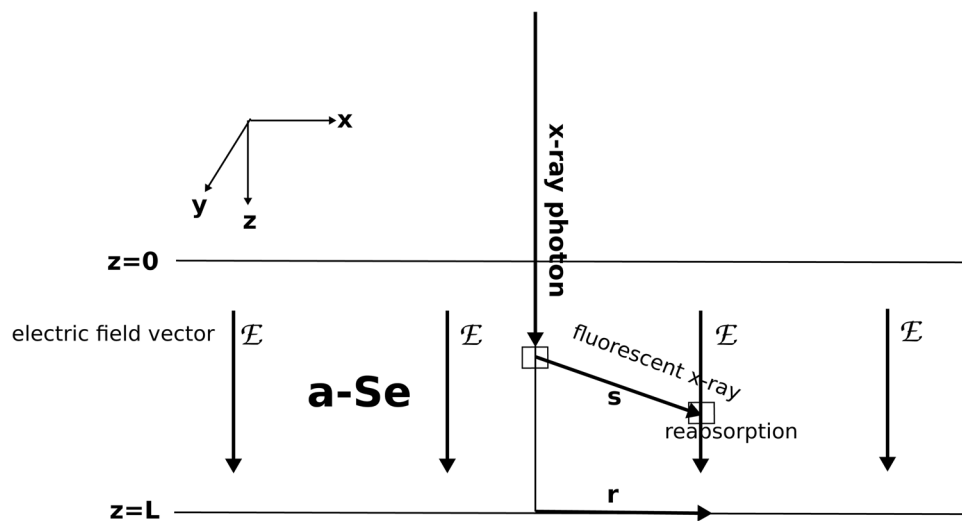

FIG. 3. Geometry for calculation of the K-fluorescent re-absorption. The fluorescence is assumed isotropic and a vertical (z) electric field moves charges to the detection plane with negligible blurring due to diffusion and the space charge effect.
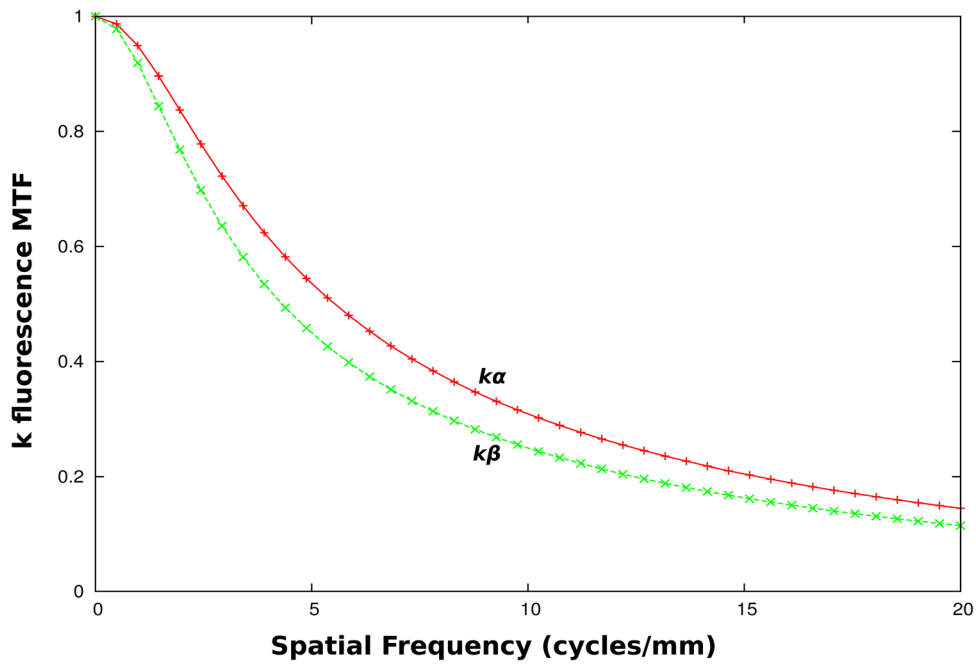
FIG. 4. MTF_α and MTF_β due to the reabsorption of K_α and K_β fluorescent radiation. The MTF_α is higher than MTF_β because the K_α radiation is lower in energy and thus is more highly attenuated due to the gradual increase which occurs in the photoelectric attenuation coefficient below the K-edge. The plots do not include the effects of the sampling aperture.

deposited at this site. This assumption is valid because the photoelectron range is very small at the low energies where the coherent cross section is the largest. The coherent scatter cross section does not change much just above and below the K-edge. Because there is a large increase in the photoelectric effect just above the K-edge, the coherently

scattered radiation is therefore more sharply attenuated and less signal blurring occurs. This is opposite to the situation that occurs with the K-fluorescent effect, where resolution is reduced above the K-edge.

The equation quantifying the coherent scatter point spread function is given by:
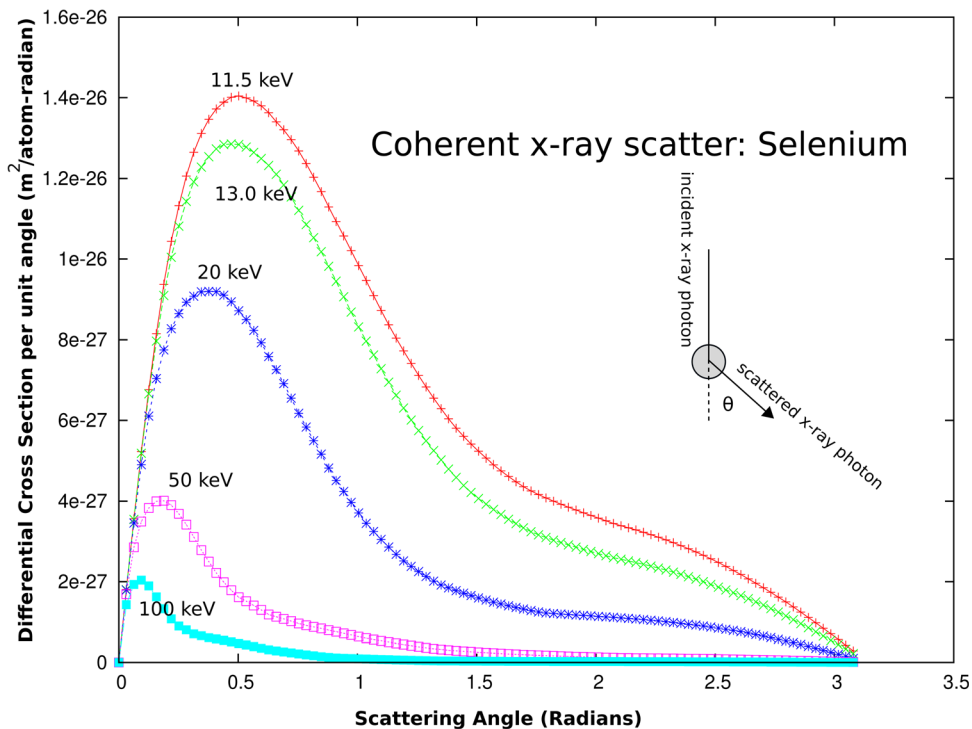

FIG. 5. Coherent scattering differential cross section. The area under each of the curves represents the total cross section for that energy.
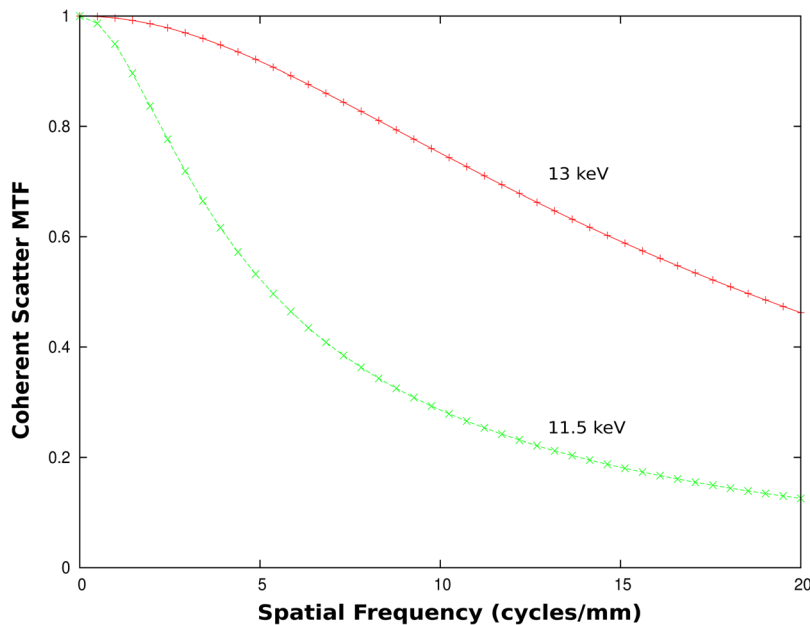
Fig. 6. Coherent scatter MTF at 11.5 and 13.0 keV. Only single scattering is considered and the coherently scattered radiation is assumed to be absorbed by the photoelectric process. Therefore just below the *K*-edge the radiation scatters farther and the coherent scattering MTF decreases. The plots do not include the effect of the sampling aperture.

$$PSF_{coh}(r) = C2 \int_0^L \int_0^L \frac{\exp(-\mu z' - \mu s)}{s^2} \frac{r_0}{2} (1 + \cos^2\theta)$$
$$\times [F(\theta)]^2 2\pi \sin\theta \, dz dz', \tag{6}$$

where $\cos\theta = (z - z')/r$, r_0 is the classical electron radius, $C2$ is a constant, and $F(\theta)$ is the angular coherent scatter form factor for Se as tabulated by Hubbell.[12] Shown in Fig. 6 are coherent scatter MTFs above and below the *K*-edge of selenium.

Incoherent or Compton scattering is also evaluated in our model but it is not a significant factor at the lower energies which we have experimentally tested. For completeness we show in Fig. 7 the behavior of the Compton scattering MTF_C at three energies.

II.D. Other effects: Diffusion, blocking layer, CCD charge transfer efficiency

The magnitude of the effect on resolution loss, due to other fundamental processes such as charge diffusion and space charge repulsion are very minor. Nonetheless, we did investigate the effect of charge diffusion. We found that the MTF reduction at 20 cycles mm^{-1} for a 200 μm thick a-Se layer is 1% at an x-ray energy of 20 keV when the electric field is 10 V μm^{-1} or 3% if the field is only 3 V μm^{-1}. These results were calculated using the equation[17] derived by Que and Rowlands which pertains to charge being collected on a del/pixel plane rather than at the surface of the a-Se which is closest to the x-ray source.

The fraction of the *K*-fluorescent and Compton scattered radiation reabsorbed by the a-Se layer (200 μm) was calculated using methods similar to those discussed in Que and Rowlands.[3] Because the coherent scattering is largely forward peaked and the a-Se layer is thick it was assumed all of the coherently scattered radiation was reabsorbed. It is recognized that this assumption starts to break down at energies greater than 50 keV. A future refinement to the existing

model would be to take into account the escape fraction of the forward peaked coherent radiation. A plot of the relative signal weighting factors $w_{pe}, w_{Auger}, w_\alpha, w_\beta, w_{coh}, w_C$ for the different processes as a function of x-ray energy is shown in Fig. 8. Note that the weighting factors were evaluated exactly for each energy at which the MTF was evaluated. The plot in Fig. 8 shows only representative points.

In all of the considerations thus far, it has been assumed that the signal charges in the a-Se layer move vertically in the a-Se layer (thickness L) and that the effective signal collected at the pixellated signal plane is generated directly with no lateral charge/signal spreading due to electric field distortions. However, for various reasons it is possible that the a-Se layer adjacent to the discrete signal collection electrodes can trap charge. This would distort the electric field in the blocking layer above the signal electrodes. The trapping of the carriers in the bulk of a-Se itself was neglected because charge transport measurements indicated excellent charge carrier ranges, typical of good quality a-Se.[13] The a-Se used as the photoconductor was prepared to have long electron lifetimes.[14] From a signal point of view it is possible to model such effects as if the signal charge is trapped a fixed distance l above the signal plane.[4,15] For easy visualization, and to a good first approximation, the electric field caused by a point signal charge above the blocking layer (l can be viewed as a dipole field due to the signal charge and a mirror charge of opposite sign a distance $-l$ below the signal electrode plane. The full solution of this signal blurring effect, which includes the effects of the bias electrode on the surface of the a-Se layer (which induces an infinite series of image charges), is:

$$MTF_{bl} = \frac{L \sinh(2\pi\nu(L - l))}{(L - l) \sinh(2\pi\nu L)}. \tag{7}$$

For the detector that was used to measure *MTF* as a function of energy it was found that the measured *MTF* was significantly lower than the theoretically possible *MTF*. As will be
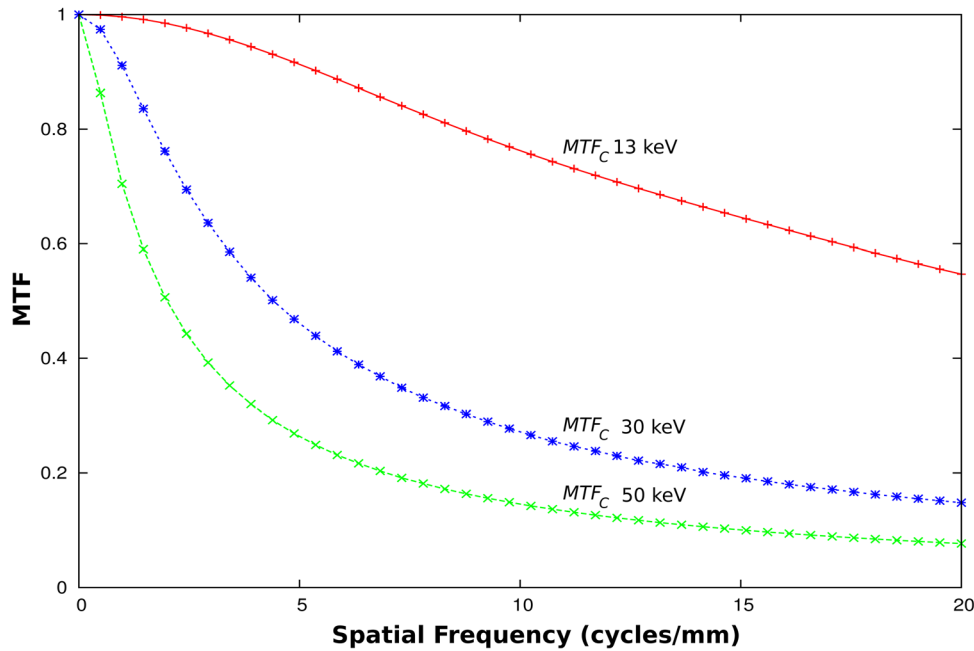
FIG. 7. Compton scattering MTF_C at 13.0, 30.0, and 50 keV. The plots do not include the sampling aperture.

seen in an examination of the experimental data in Sec. IV B, the choice of a suitable blocking layer thickness l, brings the experimental results into close agreement with the expected theoretical behavior.

The charge image within the CCD is vertically and horizontally shifted to a charge to voltage converter amplifier at the periphery of the CCD. The charge transfer process is not perfect and leads to image blur. According to Theuwissen,[16] the MTF due charge transfer inefficiency, is given by

$$MTF_{cte}(\nu) = \exp\left(-\epsilon_m N\left[1 - \cos\left(\pi\frac{\nu}{\nu_N}\right)\right]\right), \qquad (8)$$

where ϵ_m is the charge transfer inefficiency, and N is the number of transfers. The charge transfer efficiency, CTE, is given by $1 - \epsilon_m$. The CTE can be estimated from the extended pixel edge response.[17]

The expected value of the measured MTF is given by

$$MTF(\nu) = MTF_w(\nu)MTF_{bl}(\nu)MTF_{cte}(\nu)MTF_\alpha(\nu), \qquad (9)$$

where $MTF_a(\nu) = \frac{\sin(\pi a\nu)}{\pi a\nu}$ is the MTF associated with the aperture width a of the detector element.

III. MATERIALS AND METHODS

III.A. a-Se base CCD detector

The small image readout device utilized a custom designed CCD made by the DALSA corporation (Kitchener-Waterloo Ontario). The CCD image area was 5×10 mm with a 25 μm del (detector element) pitch yielding a total of 200×400 dels. The CCD utilizes a four phase clocking structure with a horizontal readout register containing 200 image transfer storage elements. The CCD was fabricated on
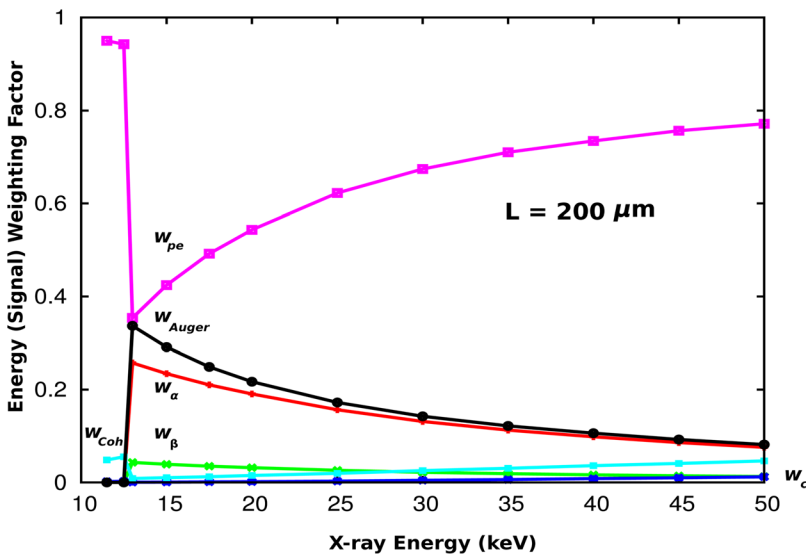

FIG. 8. MTF energy (signal) weighting factors. The most important factors affecting the MTF are the photo-lectron w_{pe} and fluorescent w_α factors. The w_{Auger} factor is also large but the effective range of the Auger-electrons ($\sim$12 keV) is very short ($\sim$0.43 μm) and does not reduce the MTF significantly. The coherent scatter w_{coh} and fluorescence w_β are of nearly the same importance at the lowest energies of interest (12 keV) while Compton scatter, w_C, remains of little importance up to energies of at least 50 keV.
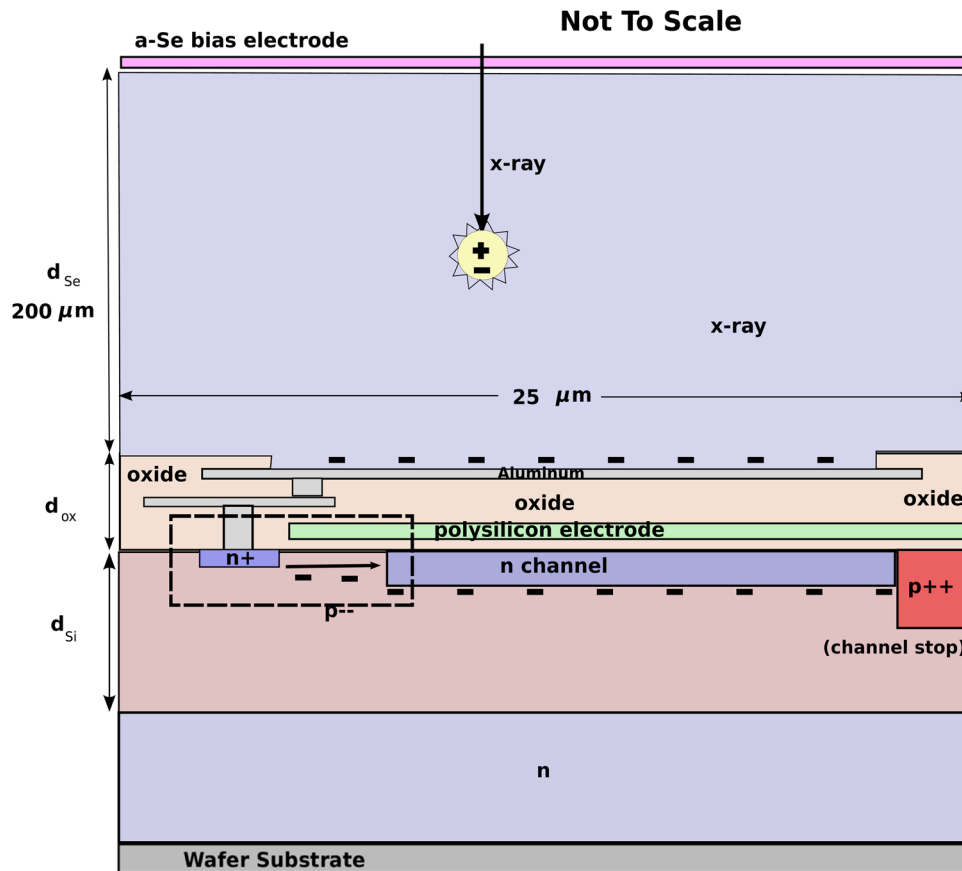
Not To Scale

FIG. 9. Cross section (not to scale) of the CCD (four phase) del structure showing a polysilicon phase one electrode which also acts as a MOSFET gate to transfer a negative signal from the a-Se layer into the n-channel. The del pitch is 25 μm and the a-Se layer was 200 μm thick for the specific detector used for the measurements. The a-Se bias electrode was held negative with respect to the wafer substrate. The bias electrode is estimated to absorb less than 1% of the incident radiation at 11.56 keV. The region center left of the diagram within the boxed area (dashed) is the effective MOSFET signal input structure. The equivalent circuit of CCD signal generation and capture can be seen in Fig. 10.

a p-doped epitaxial layer with a standard n-doped implant structure to implement buried channel operation for an electron signal. The electron signal developed in the a-Se layer deposited on top of the CCD die was transferred to the individual CCD dels by means of a MOSFET input structure as depicted in the dashed box in Fig. 9. The device is designed

to work in the time delay integration (TDI) mode,[18] but for the measurements presented here the images were taken with a single exposure frame (200 × 400) and were read out after each x-ray exposure as a single frame. The equivalent circuit of the x-ray signal generation and capture within the CCD is shown in Fig. 10.
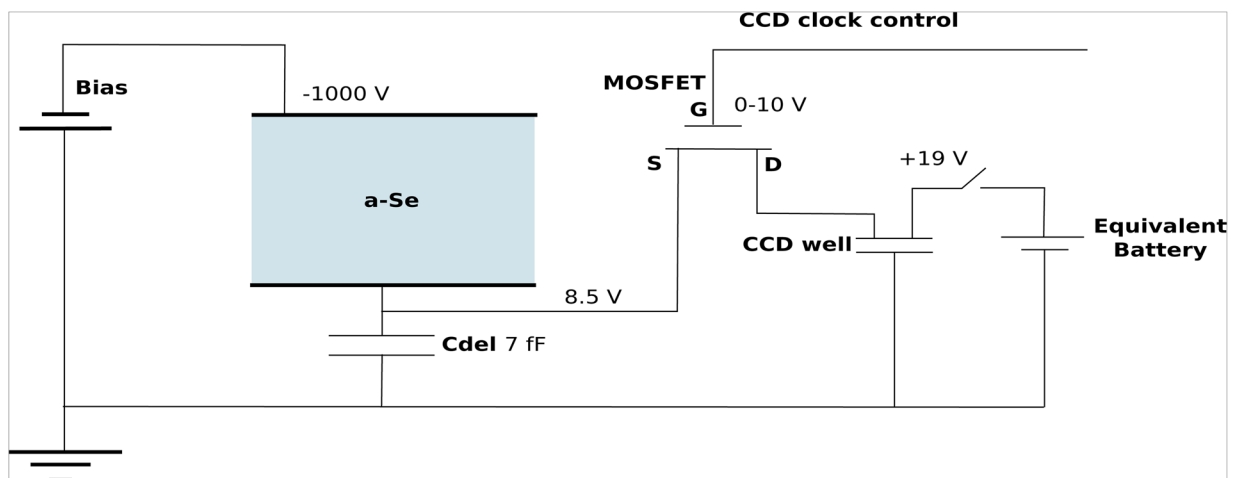

FIG. 10. The a-Se and CCD equivalent circuit. The values of the voltages and capacitances are representative and estimated, respectively. The "MOSFET" charge transfer switch is the key element involved in transferring the x-ray signal charge developed in the a-Se layer into the CCD signal well(s).

The operation of the MOSFET charge transfer switch shown in Figs. 9 and 10 can introduce nonlinear signal transfer characteristics at low x-ray signal levels. The x-ray threshold of operation is lowered by reducing the value of the capacitance (C_{del} as shown in Fig. 10) and by increasing the sensitivity of the a-Se layer by using the highest possible bias field across the a-Se.

III.B. Control electronics

The electronics controlling the CCD device were built specifically for the custom device and were implemented using CPLD (custom programmable logic devices), MOSFET drivers for the CCD clock lines, an emitter-follower amplifier for amplifying the CCD output signal, a 14 bit digitizer with built in correlated double sampler, plus other associated logic. The image data were captured in a PC frame grabber communicating with the CCD data acquisition board via an LVDS (low voltage differential signal) cable.

III.C. Selenium deposition

A Se:0.2% As alloy was used to form a stabilized amorphous-selenium (a-Se) layer on the upper surface of the CCD die. The doping levels and the composition of the a-Se was chosen to obtain the best transport properties and prevent trapping in the bulk of the photoconductor. A suitable mask was made to restrict evaporation of the a-Se to only the active image area of the CCD. The selenium was vacuum deposited as described elsewhere.[19] Wire bonding of the device into a chip carrier platform was performed at the NOVA corporation (San Diego, CA).

III.D. Monochromatic x-ray source and imaging procedure

The measurements with nearly monochromatic x-rays were performed at 05B1-1 beamline, Canadian Light Source Inc. By adjusting the angulation of the crystals, the energy and intensity of the x-ray beam were adjusted. Images were made with energies ranging from 11.5 to 30 keV. It is estimated that at all energies employed, the contribution of high order diffraction harmonics was 1% or less. The CCD, mounted on the electronics board, was placed at a distance of approximately 13 m from the monochromator apparatus. The beam is nearly parallel and is nominally 0.85 cm high and 20 cm wide. The length of the exposure was controlled by a relay activated shutter with a reproducible response time of ~40 ms. The typical x-ray exposure time was 200 ms. The bias applied to the a-Se was varied between −500 and −700 V.

A tantalum bar 16.8 mm wide, 0.25 mm thick, and 106 mm long was used to make edge images with the CCD. The bar was pressed against a support frame located over the CCD. The tantalum edge was moved in and out of position over the CCD by means of a stepper stage. The spacing of the edge from the CCD image surface was about 1 cm, small enough that beam divergence effects of the beam on the resolution should be negligible This was shown to be true by

imaging a pointed object several meters away from the CCD. No loss of resolution of the point was apparent. The edge was positioned such that it was at an angle of ~2° to the del scan direction(s).

Prior to forming an edge image at a given energy and monochromator settings, the tantalum edge was completely removed from the active image area and ten sequential dark and ten x-ray images (20 in total) were taken in order to create a gain variation map to flat-field subsequent x-ray images.

The tantalum edge was then appropriately positioned in front of the CCD and several edge images at that energy were acquired. The procedure of flat-fielding and edge image acquisition was carried out for all of the energies of interest. After the edge images were acquired the slanted edge technique[20] was used to determine the MTF. A nonlinear optimization transform[21] was applied to the synthesized images to help reduce spurius high frequency spatial noise. The correctness of the algorithms used to determine the MTF were verified by testing with synthesized edges with known properties.

IV. RESULTS AND DISCUSSION

IV.A. a-Se CCD operating characteristics

IV.A.1. CCD: dark response, x-ray signal transfer, CTE

The dark response of the CCD is shown in Fig. 11. The dark response is measured by stopping the readout CCD clocks for a specified period of time and then reading out an image frame. The applied a-Se bias was limited to a maximum of −700 V. This limit was primarily imposed to prevent breakdown in air and to limit small image defects caused by a poor bias electrode formation. Future devices will be prepared in such a way as to make this restriction unnecessary. For the applied a-Se biases, the dark response was due to thermal charge carrier creation within the CCD, with negligible contribution from the a-Se bias. As can be seen the dark response is a linear function of the silicon
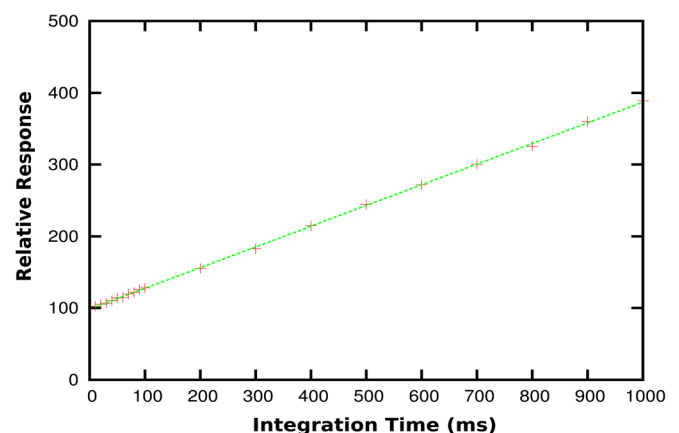
Fig. 11. The CCD dark response, measured by increasing the integration period when the CCD clocks are suspended. The dark response was primarily due to thermal carrier production within the CCD, with a negligible contribution from the biased a-Se layer.
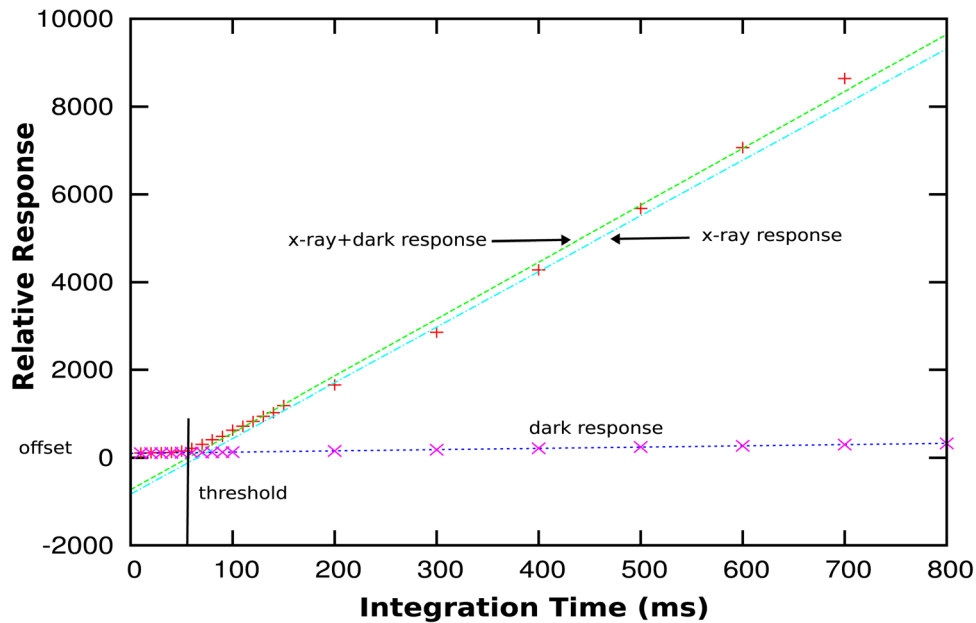
FIG. 12. The CCD x-ray response to increasing x-ray exposure attained by increasing the exposure time. There is a threshold x-ray level before the detector shows an increased response. This is due to the threshold of the MOSFET switch (Figs. 9 and 10). Thereafter the response is approximately linear. The maximum integration time corresponds approximately to 4.7 mGy.

(CCD) thermal carrier generation time, which demonstrates that signal readout from the entire electronics signal chain is linear.

The relative x-ray response was characterized by increasing the x-ray exposure time using a tungsten target mammography x-ray tube, while keeping the tube current and kV constant. The x-ray exposure time was varied from a few milliseconds to nearly a full second. The results obtained are shown in Fig. 12. The exposure rates employed were comparable to those used with the monochromatic sources. The threshold response is caused by the failure of the MOSFET transfer switch to turn on at low signal levels. Above the x-ray threshold the device works nearly linearly, although the linear range of operation is compromised by the relatively high threshold of operation of the MOSFET switches.

The *CTE* was determined using the extended pixel edge response given by

$$CTE = 1 - \frac{S_d}{SN}, \tag{10}$$

where S_d is the deferred charge value,[17] S is the signal level in the last column, and N is the number of charge transfers. Dark response images were used to determine the *CTE*. An estimate of the *CTE* evaluated by this method was $\sim$0.9992 for both the horizontal and vertical directions. The values of the *CTE* are not particularly good and they can in part be related to the MOSFET input structure and suboptimal operation of the CCD clocks. The value of N was taken as 200 for the horizontal direction and 400 for the vertical direction.

IV.A.2. CCD image results

Shown in Fig. 13 are two images of lead bar patterns obtained with a polychromatic x-ray spectrum from a

tungsten target x-ray tube operated at 45 kV. The 5 lp/mm image on the left is "raw" while the 10 lp/mm image on the right has been "flat-fielded". The beam was filtered with 30 μm of molybdenum. Vertical artifacts related to the polysilicon CCD electrode structures can be seen in the left image. Other imperfections are also visible. Vertical edge images were analyzed since the effect of the *CTE* is less in the
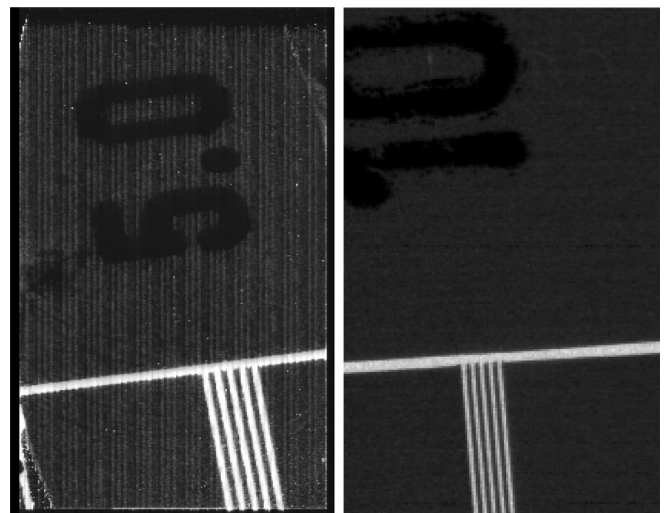

FIG. 13. Sample CCD x-ray images of a lead bar test pattern. The image on the left of is of a 5 lp/mm bar pattern segment and it is "raw", while the image on the right has been "flat-fielded" and is of a 10 lp/mm segment of the bar pattern. The dark patch at the center left of the left image is the region where the high voltage wire was attached to the a-Se bias electrode with a conductive adhesive compound. The vertical patterns in the images are associated with the polysilicon electrode structure of the CCD. The images were taken with a polychromatic x-ray beam from a tungsten target x-ray tube operated at 45 kV with 30 μm of molybdenum filtration.
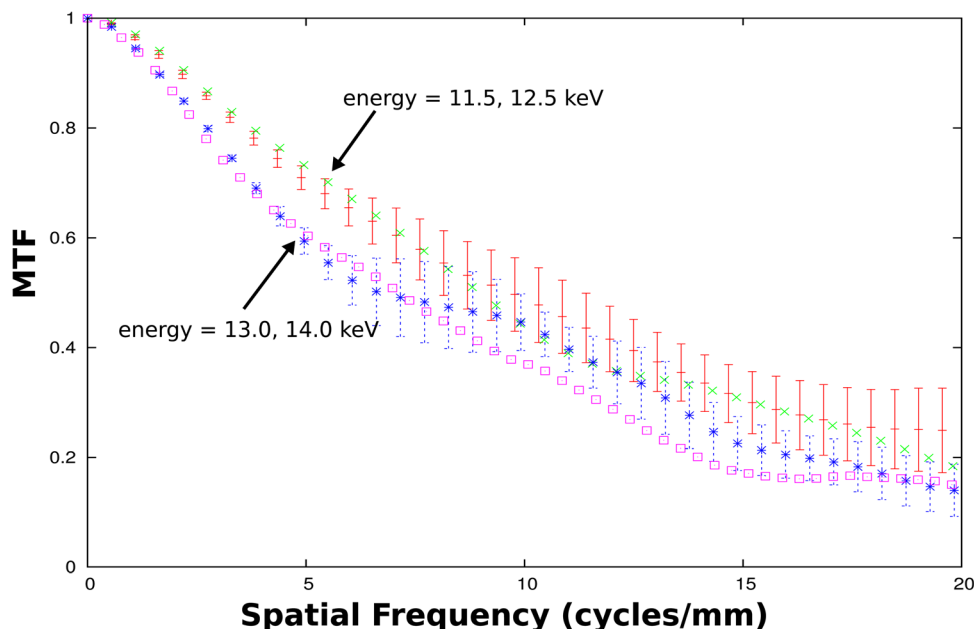
FIG. 14. a-Se CCD prototype MTF results obtained from tantalum edge images. The results for 11.5, 12.5, 13.0, and 14.0 keV are shown. The sampling aperture is 25 μm. It is evident that there is a noticeable drop in the MTF at energies above the *K*-edge.

vertical direction due to the smaller number of charge transfers required in the horizontal direction. It can be seen that the flat-fielding has suppressed the vertical artifacts. It is recognized that the flat-fielding cannot correct for the threshold operation of the MOSFET input structure at low signal levels. However, the threshold operation should have only the effect of reducing low frequency content due to poor signal response in the low signal part of the edge image.

IV.B. MTF results

Shown in Fig. 14 are the principal results indicating the effect of *K*-fluorescence in a-Se imaging. Each MTF plot at a given energy was obtained from 12 image edge locations spaced vertically about 10 del positions apart. It is clear that the quality of the images is not sufficiently high to give results without artifacts concerning the change in resolution above and below the *K*-edge of selenium above about 10 cycles mm^{-1}. However, below 10 cycles mm^{-1} it is clear that the change in MTF is in agreement with the trend expected from theory. We consider that the high spatial frequency noise (above 10 cycles mm^{-1}) is caused by spatially varying dark currents associated with the bias electrode. Shown in Fig. 15 are the theoretical predictions for the MTF of a a-Se detector at 12.5 and 13.0 keV. Note that the effect of the 25 μm sampling aperture, the *CTE*, and a blocking layer are included in the plots. The theoretical prediction has only one free parameter: the thickness of the blocking layer. Based on an examination of the data in Fig. 14 and theory we have estimated that the CCD device had an effective blocking layer thickness of 6 μm.

The theoretical MTF calculated with the estimated 6 μm thick blocking layer, and the effects of the aperture and CTI, shown in Fig. 15, shows reasonable qualitative and

quantitative behavior when compared with the experimental data of Fig. 14. The expected MTF results without the effects of a blocking layer and the CTE are shown in Fig. 16. Based on the method of selenium deposition, we expected the effective blocking layer thickness to be less than the value of 6 μm, the value of which we have inferred from our MTF results. We have no explanation for this. It is possible that the resolution is compromised due to some other unforeseen mechanism. It is clear that the spatial resolution performance of our current device, although good, is far from what can be achieved theoretically.

Shown in Fig. 15 are the theoretical predictions of the MTF at 12.5 and 13.0 keV assuming a blocking layer thickness of 6 μm. Comparison with the experimental results as shown in Fig. 14 shows reasonable agreement.
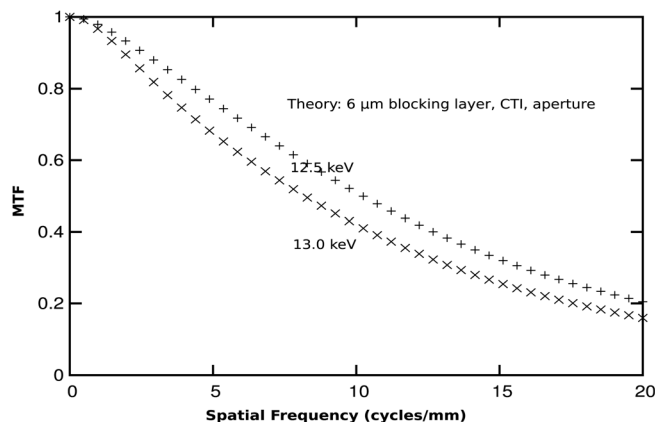

FIG. 15. Theoretical MTF predictions for the MTF at the two energies: 12.5 and 13.0 keV using 1 free parameter: a 6 μm thick blocking layer. The plots include the effect of the 25 μm sampling aperture and the effect of the *CTE*.
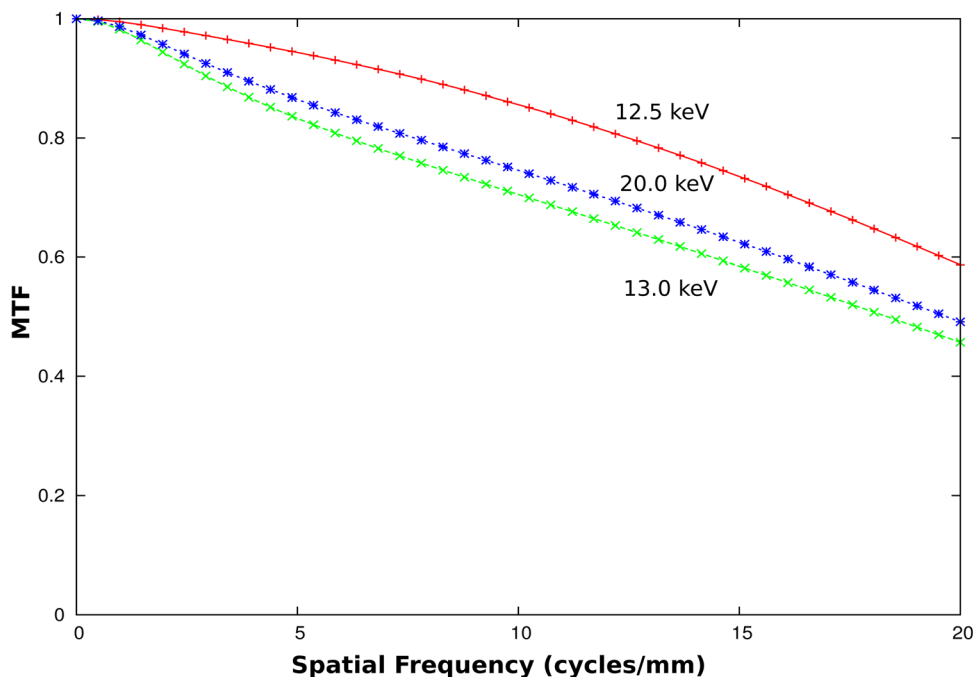
FIG. 16. The theoretically possible MTF with a-Se with a 25 μm pitch sampling system in the mammographic energy range. The effects of the sampling aperture are included.

V. CONCLUSIONS

We have experimentally measured the MTF at different monochromatic energies of an a-Se imaging prototype x-ray CCD detector with a Nyquist sampling frequency of 20 cycles/mm and found a reduction of the MTF above the K-edge of selenium. We have outlined a general theory, based in part upon the work of previous authors,[3] which predicts the expected spatial resolution (MTF) of a-Se imaging devices over the diagnostic energy range (2–200 keV). Although we are primarily interested in the region of mammographic energies, where the range of the photoelectron causes negligible MTF loss, we have also shown in the appendix how the MTF reducing effects of the range of photoelectrons can be calculated efficiently, without Monte Carlo methods, by using electron range and depth-dose profile parametric models available in the literature.[11] The theory as developed here also incorporates an electrostatic blurring mechanism which appears to be needed to explain the lower resolution obtained with the prototype device than that for an ideal "perfect" a-Se detector. It is possible there are other mechanisms associated with the operation of the detector structure which we have not taken into account.

We have compared the experimental MTF results with theoretical MTF calculations and we have achieved agreement provided the detector prototype, sampling aperture 25 μm, is assumed to have a 6 μm charge trapping blocking layer. Thus, in future high resolution ($\geq$20 cycles mm) a-Se based x-ray imaging detectors, the effect of blocking layers will need to be carefully managed to attain the maximum MTF permitted by the x-ray physics of selenium. It is also clear that the threshold operation of the MOSFET charge input switch is a problem which requires minimization or a different charge transfer mechanism that does not require a MOSFET should be considered.

APPENDIX: RANGE OF THE PHOTELECTRON

The mechanics of the photoelectron have been addressed in Evans,[22] Johns and Cunningham,[23] Attix,[24] Knoll,[25] Que and Rowlands,[3] and elsewhere. The energy loss of a photoelectron occurs principally by ionization caused by collisions between the energetic electrons and bound Se electrons, with the final low energy thermalization presumably occurring through the creation of phonons. Since the masses of the two interacting particles are identical, at most half of the energy can be transferred in a single collision.[23] A small energy loss also occurs by Bremsstrahlung radiation when an electron is accelerated near an atomic nucleus, but for energies below 100 keV this contribution is negligible. Shown in Fig. 17 is a representation of the physics involved and the three distance
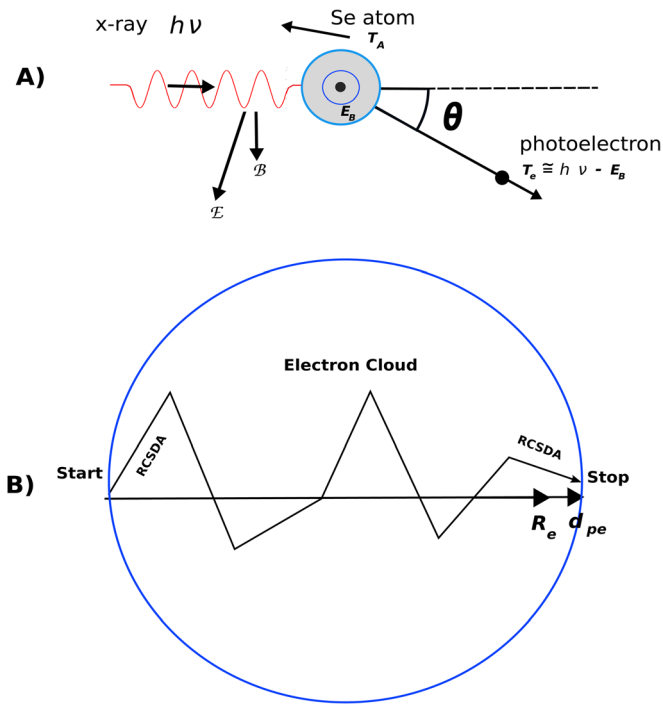
FIG. 17. (A) Photoelectron ejected after a selenium atom has interacted with a photon with energy greater than E_B of the K-shell. (B) Conceptual illustration of the difference between the R_{CSDA} and the penetration distance d_{pe} of an energetic electron. The value of d_{pe} is close to the extrapolated range R_e, which is defined in the text. For Se we take the ratio $\frac{R_{CSDA}}{R_e} = 2.0$ which is based on analytical fitting to Monte Carlo results[11] and supported by experimental data[26,27] obtained from Ge samples; Ge being physically similar to Se. The extrapolated range R_e (defined in the text) is also shown. In general $R_e < d_{pe} < R_{CSDA}$.

parameters R_{CSDA} R_e d_{pe} of interest. The primary distance of interest, d_{pe}, is the farthest distance photoelectrons appear from the initial photoelectric interaction site. The remaining two distances are defined shortly. The deposition of energy along the electron path(s) shown in Fig. 17B) will not be uniform, with more energy being released midway in the path than at the beginning or end of the path. The initial increase in energy deposited with pathlength can be attributed to the geometric growth of the number of electrons participating in the ionization processes and the tailing decrease of energy transfer as due to the thermalization of the final lower energy free charges created.

One efficient method to estimate the electron range is to use the continuous-slowing-down approximation (CSDA). The pathlength R_{CSDA} using this method is also known as the Bohr-Bethe[28] range. The value of R_{CSDA} is given by

$$R_{CSDA} = \int_0^E \frac{dE}{S(E)} \tag{A1}$$

where $S(E)$ is the average stopping power and E is the initial kinetic energy. As can be seen in Fig. 17, the value of R_{CSDA} will always be larger than the penetration distance d_{pe} the electron travels. For a given material it is assumed that $R_{CSDA} = k d_{pe}$ where K is a constant, a detour factor. Through an on-line program[29] "ESTAR" provided by the NIST we have determined R_{CSDA} of a-Se ($\rho = 4.26$ g cm^{-3}) for the range of energies relevant to our study (2–200 keV). As discussed in Ref. 3 one must consider the ratio of R_{CSDA} to the extrapolated range d_{pe} which the photoelectron travels in order to calculate the MTF loss due to d_{pe}. This "K" factor
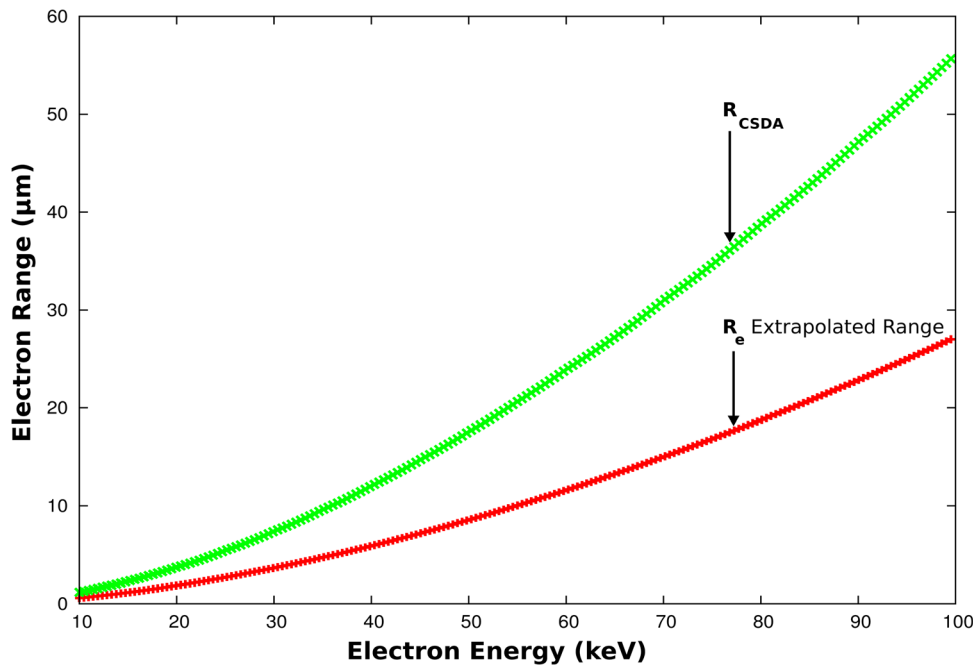

FIG. 18. Normalized selenium depth-dose plotted using Eq. (A3) where $A = 0.3, B = 13, C = -5, D = 10, E = 1, F = 3$. Shown inserted is the extrapolated range R_e. It is assumed that because of slight errors in extracting the fitting parameters from the published plots,[11] the value of R_e is not exactly 1.0. The value of $R_e \le d_{pe}$, but for practical reasons and since most of the energy is deposited at values $<d_{pe}$, R_e is the parameter of interest.
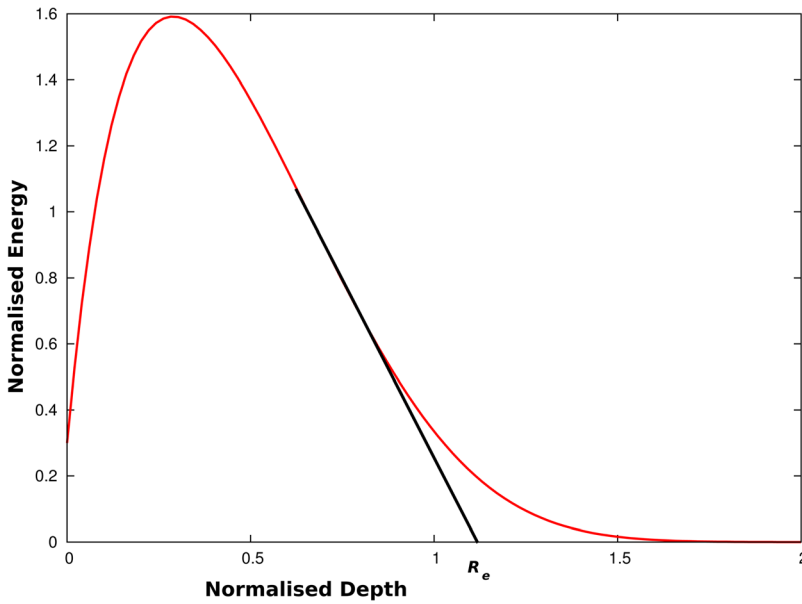
FIG. 19. Plots of the electron ranges R_{CSDA} and the extrapolated electron range R_e as determined using Eqs. (A1) and (A2). The ratio $\frac{R_{CSDA}}{R_e}$ remains constant at the value 2.0 over the plotted energy range.

was estimated by Que and Rowlands to have a value of ~ 2. Using methods outlined below we have found the value to be almost exactly 2.0 when a parameter (defined later) called R_e, the extrapolated range ($R_e \propto d_{pe}$), is used instead of d_{pe}. Furthermore $\frac{R_{CSDA}}{R_e}$ is found to have very little energy dependence within the range of energies we are concerned with.

The range and energy deposition profiles of electrons can be determined by numerically intensive Monte Carlo procedures. Kim *et al.*[11] have developed excellent empirically fitted functions of extrapolated electron ranges R_e, and energy deposition (dose) profile data as obtained from Monte Carlo simulations.[30] The value of R_e is defined as the point where an extrapolation of the straight-line segment of the depth-dose curve intercepts the depth abscissa as shown in Fig. 18. The value of $R_e \leq d_{pe}$. For a given atomic number, both R_e and the normalized depth-dose, $g(w)$, can be normalized with respect to the energy E. This means that the shape of the depth-dose curve, for a given element, is parameterized in such a way as to be invariant with E. The normalization condition is $\int_0^\infty g(w)dw = 1$ where $w = \frac{x}{S_x}$, $g(w) = \frac{D(x)}{S_y}$ and S_x and S_y are the appropriate scaling factors for the depth and dose axes, respectively. The empirical fit by Kim *et al.* for the electron extrapolated range is given by:

$$R_e = \alpha(x)E_i^{\beta(z)}, \tag{A2}$$

where $\alpha(z)$ and $\beta(z)$ are functions of the atomic number z. Examining their plots, we estimate the value of $\alpha(34)$ and $\beta(34)$ to be ~ 5.3 and 1.67, respectively. We show plotted in Fig. 19, both R_{CSDA} and R_e as determined by Eqs. (A1) and (A2), respectively. The ratio $\frac{R_{CSDA}}{R_e}$ remains very close to the value of 2.0 over the entire energy range. The empirical depth-dose profile is given as

$$g(w) = \{A(z)+B(z)w+C(z)w^2+D(z)w^3\}e^{-\{E(z)w^3+F(z)w\}} \tag{A3}$$

and upon examination of the plots in Ref. 11, we estimate that for selenium

$$A(34) \simeq 0.3, B(34) \simeq 13, C(34) \simeq -5,$$
$$D(34) \simeq 10, E(34) \simeq 1, F(34) \simeq 3.$$

Shown plotted in Fig. 18 is the normalized depth-dose curve for electrons of energy E impinging upon a slab of a-Se. We realize that the situation is not exactly the same as for the emission of a high energy electron within the bulk of an a-Se layer by the absorption of an x-ray photon. Nonetheless to estimate the loss of resolution due to the creation of an ionization charge cloud created by the photoelectron we proceed by simply modeling the charge distribution as a Gaussian function $\exp\left(\frac{-r^2}{\sigma^2}\right)$, where $\sigma = \frac{R_e}{2}$ and r is the radial distance from the initial photoelectron interaction site. Note that this is equivalent to setting $\sigma = \frac{R_{CSDA}}{4}$ where our analysis has introduced an additional factor of 1/2 compared to the more conservative estimate of Que and Rowlands which overestimates the effect of the photoelectron range. Based on these assumptions, we show in Fig. 2, the (unweighted) value of the photoelectron MTF_{pe} which is proportional to the function $\exp(-\pi^2\nu^2\sigma^2)$ (Ref. 3) where ν is the spatial frequency.

At lower energies ($E < 80$ keV) the range of the photoelectron has little impact on resolution. It is not until $E \gtrsim 80$ keV that the photoelectron range becomes significant as is shown in Fig. 2. Therefore for the experimental energies tested in this study (11.5–30.0 keV), the size of the ionization cloud produced by the photoelectrons is not important. Refer to Fig. 2 in Sec. II A to view MTF_{pe}.

a)Electronic mail: david.hunter@sri.utoronto.ca

[1] S. Rivetti, N. Lanconelli, M. Bertolini, G. Borasi, P. Golinelli, D. Acchiappati, and E. Gallo, "Physical and psychophysical characterization of a novel clinical system for digital mammography," Med. Phys. **36**, 5139 (2009).

[2] S. Rivetti, N. Lanconelli, M. Bertolini, and D. Acchiappati, "A new clinical unit for digital radiography based on a thick amorphous Selenium plate: Physical and psychophysical characterization," Med. Phys. **38**, 4480 (2011).

[3]W. Que and J. A. Rowlands, "X-ray imaging using amorphous selenium: Inherent spatial resolution," Med. Phys. **22**, 365–374 (1995).

[4] D. M. Hunter, G. Belev, G. DeCrescenzo, S. O. Kasap, J. G. Mainprize, J. A. Rowlands, C. Smith, T. Tumer, V. Verpakhovski, S. Yin, and M. J. Yaffe, "The dependence of the modulation transfer function on the blocking layer thickness in amorphous selenium x-ray detectors," Med. Phys. **34**, 3358 (2007).

[5]S. Kasap, J. B. Frey, G. Belev, O. Tousignant, H. Mani, J. Greenspan, L. Laperriere, O. Bubon, A. Reznik, G. DeCrescenzo, K. S. Karim, and J. A. Rowlands, "Amorphous and polycrystalline photoconductors for direct conversion flat xanel x-ray image sensors," Sensors **11**, 5112–5157 (2011).

[6]J. M. Boone, J. A. Seibert, J. M. Sabol, and M. Tecotzky, "A Monte Carlo study of x-ray fluorescence in x-ray detectors.," Med. Phys. **26**, 905–916 (1999).

[7]W. Zhao, W. G. Ji, and J. A. Rowlands, "Effects of characteristic x rays on the noise power spectra and detective quantum efficiency of photoconductive x-ray detectors," Med. Phys. **28**, 2039 (2001).

[8]G. Hajdok, J. Yao, J. J. Battista, and I. A. Cunningham, "Signal and noise transfer properties of photoelectric interactions in diagnostic x-ray imaging detectors," Med. Phys. **33**, 3601 (2006).

[9]G. Hajdok, J. J. Battista, and I. A. Cunningham, "Fundamental x-ray interaction limits in diagnostic imaging detectors: Spatial resolution," Med. Phys. **35**, 3180 (2008).

[10]W. Heitler, *The Quantum Theory Of Radiation*, 3rd ed. (Dover, New York, 1984).

[11]W. Kim, I. Jun, and H. B. Garrett, "An algorithm for determining energy deposition profiles in elemental slabs by low (<100 keV) energy electrons: An internal charging application," IEEE Trans. Nucl. Sci. **55**, 3158–3163 (2008).

[12]J. H. Hubbell, W. J. Veigele, E. A. Briggs, R. T. Brown, D. T. Cromer, and R. J. Howerton, "Atomic form factors, incoherent scattering functions, and photon scattering cross sections," J. Phys. Chem. Ref. Data **4**, 471–538 (1975).

[13]S. Kasap, J. B. Frey, G. Belev, O. Tousignant, H. Mani, L. Laperriere, A. Reznik, and J. A. Rowlands, "Amorphous selenium and its alloys from early xeroradiography to high resolution x-ray image detectors and ultrasensitive imaging tubes," Phys. Status Solidi B **246**, 1794–1805 (2009).

[14]S. O. Kasap, K. V. Koughia, B. Fogal, G. Belev, and R. E. Johanson, "The influence of deposition conditions and alloying on the electronic properties of amorphous selenium," Semiconductors **37**, 789–794 (2003).

[15]W. Zhao, W. G. Ji, A. Debrie, and J. A. Rowlands, "Imaging performance of amorphous selenium based flat-panel detectors for digital mammography: Characterization of a small area prototype detector," Med. Phys. **30**, 254 (2003).

[16]A. J. Theuwissen, *Solid-State Imaging With Charge-Coupled Devices* (Kluwer Academic Publishers, Dordrecht/Boston/London, 1996).

[17]J. R. Janesick, *Scientific Charge-Coupled Devices* Bellingham (SPIE, Washington, 2001).

[18]J. G. Mainprize, N. L. Ford, S. Yin, T. Tumer, and M. J. Yaffe, "A slot-scanned photodiode-array/CCD hybrid detector for digital mammography," Med. Phys. **29**, 214 (2002).

[19]S. O. Kasap and G. Belev, "Progress in the science and technology of direct conversion X-ray image detectors: The development of a double layer a-Se based detector," J. Optoelectron. Adv. Mater. **9**, 1–10 (2007).

[20]E. Buhr, S. Gunther-Kohfahl, and U. Neitzel, "Accuracy of a simple method for deriving the presampled modulation transfer function of a digital radiographic system from an edge image," Med. Phys. **30**, 2323 (2003).

[21]A. D. A. Maidment and M. Albert, "Conditioning data for calculation of the modulation transfer function," Med. Phys. **30**, 248 (2003).

[22]R. Evans, *The Atomic Nucleus* (Kreiger, Malabar,1955).

[23]H. Johns and J. Cunningham, *The Physics of Radiology*, 4th ed. (Charles C Thomas, Springfield, Illinois, 1983).

[24]F. H. Attix, *Introduction to Radiological Physics and Radiation Dosimetry* (John Wiley & Sons, Inc., New York,1986).

[25]G. F. Knoll, *Radiation Detection and Measurement*, 2nd ed. (John Wiley & Sons, Inc., New York,1989).

[26]A. Makhov, "The penetration of electrons into solids," Sov. Phys. Solid State **2**, 1934–1941 (1960).

[27]A. Viatskin and A. Makhov, "Retardation of electrons into solids," Sov. Phys. Tech. Phys. **3**, 690–696 (1958).

[28]T. Everhart and P. Hoff, "Determination of kilovolt electron energy dissipation vs penetration distance in solid materials," J. Appl. Phys. **42**, 5837–5846 (1971).

[29]NIST, "Stopping-power and range tables for electrons," (2011). http://physics.nist.gov/PhysRefData/Star/Text/ESTAR.html

[30]J. Halbleib, R. Kensek, G. Valdez, S. Seltzer, and M. Berger, "ITS: The integrated TIGER series of electron/photon transport codes-Version 3.0," IEEE Trans. Nucl. Sci. **39**, 1025–1030 (1992).